

**SYNTHESIS AND CHARACTERIZATION OF
ZINC OXIDE NANORODS SENSITISED BY In_2S_3 ,
PbS AND In_2S_3 -PbS FOR
PHOTOELECTROCHEMICAL APPLICATION**

MOHAMMED RASHID OBAID ALMAMARI

UNIVERSITI SAINS MALAYSIA

2022

**SYNTHESIS AND CHARACTERIZATION OF
ZINC OXIDE NANORODS SENSITISED BY In_2S_3 ,
PbS AND In_2S_3 -PbS FOR
PHOTOELECTROCHEMICAL APPLICATION**

by

MOHAMMED RASHID OBAID ALMAMARI

**Thesis submitted in fulfilment of the requirements
for the degree of
Doctor of Philosophy**

September 2022

ACKNOWLEDGEMENT

I would not have written this thesis if it had not been for Allah's blessings being bestowed upon me. It took a lot of courage, patience, and motivation for me to accomplish my PhD thesis during the Covid-19 period. Thesis completion would not have been feasible without the following individuals' guidance, support, and help. So, with deep gratitude, I thank Dr. Naser Mahmoud Ahmed, main supervisor, for his advice, encouragement, and support. His meticulous attention to detail, and significant suggestions helped shape this thesis. His persistent support and tolerance enabled me to finish this difficult academic phase. Dr. Araa Mebdir Holi, my co-supervisor, assisted me in building the technical foundation for my project and guided me throughout my PhD studies. Her perceptive criticism, intelligent and helpful feedback, and perceptive thoughts produced this thesis. Dr. Yam Fong and Dr. Mohammed Zahir Al Abri, my co-supervisors, have been extremely supportive. Their comprehensive technical and laboratory support, along with their experience and persistent assistance, enabled me to successfully complete this research. My heartfelt appreciation goes to my mother, wife, and children. They have assisted me in overcoming the frequent bouts of loneliness that accompany being a postgraduate student away from home. This work was made possible by the SQU Nanotechnology Research Center. I would like to express our gratitude to the laboratory staff. Furthermore, for their technical, chemical, and laboratory assistance. The Universiti Sains Malaysia's, School of physics and Nano-Optoelectronics Project Laboratory (N.O.R Lab) also supported this research. Finally, I would like to express our gratitude to the Sultanate of Oman's Ministry of Higher Education, Research, and Innovation for their support of this research.

TABLE OF CONTENTS

ACKNOWLEDGEMENT	ii
TABLE OF CONTENTS	iii
LIST OF TABLES	viii
LIST OF FIGURES	x
LIST OF SYMBOLS	xviii
LIST OF ABBREVIATIONS	xix
LIST OF APPENDICES	xx
ABSTRAK	xxi
ABSTRACT	xxiv
CHAPTER 1 INTRODUCTION	1
1.1 Background of the Study	1
1.2 Problem Statement	5
1.3 Objectives.....	7
1.4 Significance of the Study	7
1.5 Scope of the Study.....	8
1.6 Thesis Outline	9
CHAPTER 2 LITERATURE REVIEW	10
2.1 Introduction	10
2.2 The Overview of Nanomaterials	11
2.2.1 Metal-Oxide Nanostructures with a 1D Structure.....	12
2.2.2 Heterostructured-Semiconductor	13
2.3 Photoelectrochemical Cell.....	15
2.3.1 Photoelectrochemical Cell Fundamental Principles.....	16
2.3.2 Quantum Confinement Theory on the Nanoscale	21
2.4 Characteristics of Zinc Oxide (ZnO).....	24

2.5	Methods for Synthesising Zinc Oxide Thin Films	26
2.6	ZnO Nanorod Array Synthesis	30
2.6.1	Vapour Phase Deposition	31
2.6.2	Metal Organic Chemical Vapour Deposition.....	32
2.6.3	Chemical Bath Deposition	32
2.6.4	Pulse Laser Deposition.....	34
2.6.5	Electrodeposition.....	34
2.6.6	Hydrothermal Method.....	35
2.7	Sensitised Semiconductor Synthesis Methods	39
2.8	Indium Sulfide Properties.....	44
2.9	Previous Works on In ₂ S ₃ /Metal Oxide Semiconductor.....	46
2.10	Lead Sulphide Properties	58
2.11	Previous Work on PbS/Metal Oxide Semiconductor.....	59
2.12	Previous Work on In ₂ S ₃ /PbS/ZnO.....	65
CHAPTER 3 METHODOLOGY		70
3.1	Introduction	70
3.2	Methods of Synthesis	70
3.3	Chemical Reagents	72
3.4	RF-Magnetron Sputtering Method for the Production of ZnO NPs.....	73
3.5	Sol-Gel Spin Coating Method for the Production of ZnO NPs.....	74
3.6	Hydrothermal Preparation of ZnO Nanorod Arrays	75
3.7	Synthesis of In ₂ S ₃ /ZnO Nanocomposites Using the SILAR Method.....	76
3.8	Synthesis of PbS/ZnO Nanocomposites via the SILAR Method.....	78
3.9	Synthesis of In ₂ S ₃ /PbS/ZnO Nanocomposites Using the SILAR Method	79
3.10	Characterisation of the Methods	79
3.10.1	Ultraviolet-visible spectroscopy.....	80
3.10.2	Powder X-Ray Diffraction	81

3.10.3	Fourier Transform Infrared Spectroscopy.....	83
3.10.4	Field Emission Scanning Electron Microscopy Analysis	84
3.10.5	Energy Dispersive X-Ray Spectroscopy	86
3.10.6	Transmission Electron Microscopy	87
3.10.7	Fluorescence Spectrometer (Photoluminescence).....	89
3.10.8	X-Ray Photoelectron Spectroscopy	90
3.10.9	Photoelectrochemical Performance.....	91
CHAPTER 4 RESULTS AND DISCUSSION OF ZnO NANOSTRUCTURES LAYERS.....		97
4.1	Introduction	97
4.2	Results and Discussion of ZnO NPs deposition by RF sputtering	97
4.2.1	Structures and morphologies of ZnO NPs	97
4.2.2	Optical characteristics of ZnO NPs.....	103
4.2.3	Photoelectrochemical performance of ZnO NPs.....	105
4.3	Results and Discussion of ZnO NPs deposition by sol-gel spin coating	107
4.3.1	ZnO NPs Structures and morphologies.....	107
4.3.2	Optical Characteristics of ZnO NPs.....	111
4.3.3	Photoelectrochemical Performance of ZnO NPs	115
4.4	Results and Discussion of ZnO Nanorod Arrays (NRAs).....	116
4.4.1	Structures and Morphologies of ZnO NRAs.....	117
4.4.2	Effects of Growth Times on Optical Properties of ZnO NRAs	124
4.4.3	XPS spectra of ZnO NRAs	128
4.4.4	Photoelectrochemical performance of the ZnO NRAs	130
CHAPTER 5 RESULTS AND DISCUSSION OF In₂S₃/ZnO, PbS/ZnO AND In₂S₃/PbS/ZnO NRAs.....		135
5.1	Introduction	135
5.2	Results and Discussion of In ₂ S ₃ /ZnO NRAs.....	135
5.2.1	Effect of Varying the Number of SILAR Cycles.....	136

5.2.1(a)	Structural Analysis	136
5.2.1(b)	Morphological Study	138
5.2.1(c)	Optical Analysis	140
5.2.1(d)	PEC Performance of In ₂ S ₃ /ZnO NRAs	143
5.2.2	Effect of SILAR Dipping Time.....	147
5.2.2(a)	Structural Analysis	147
5.2.2(b)	Optical Analysis	147
5.2.2(c)	PEC performance of In ₂ S ₃ /ZnO NRAs.....	149
5.2.3	Effect of Varying Cationic Concentration	151
5.2.3(a)	Structural Analysis	151
5.2.3(b)	Optical Analysis	152
5.2.3(c)	PEC Performance of In ₂ S ₃ /ZnO NRAs	153
5.2.4	Effect of Annealing Temperature.....	155
5.2.4(a)	Structural Analysis	156
5.2.4(b)	XPS Analysis of In ₂ S ₃ /ZnO NRs Surface.....	157
5.2.4(c)	Morphological Study	159
5.2.4(d)	Optical Analysis	164
5.2.4(e)	PEC Performance of In ₂ S ₃ /ZnO NRAs	165
5.3	Results and Discussion of PbS/ZnO NRAs.....	167
5.3.1	Effect of Varying SILAR Cycle Numbers.....	168
5.3.1(a)	Structural Analysis	168
5.3.1(b)	Morphological Study	169
5.3.1(c)	Optical Analysis	172
5.3.1(d)	PEC Performance of PbS/ZnO NRAs	173
5.3.2	Effect of SILAR Dipping Time.....	175
5.3.2(a)	Structural Analysis	175
5.3.2(b)	Optical Analysis	176
5.3.2(c)	PEC Performance of PbS/ZnO NRAs	177
5.3.3	Effect of Varying Cationic Concentration	179
5.3.3(a)	Structural Analysis	179
5.3.3(b)	Optical Analysis	180
5.3.3(c)	PEC Performance of PbS/ZnO NRAs	181
5.3.4	Effect of Annealing Temperature.....	183
5.3.4(a)	Structural Analysis	183

5.3.4(b)	XPS Analysis of PbS/ZnO NRAs Surface	185
5.3.4(c)	Morphological Study	188
5.3.4(d)	Optical Analysis	189
5.3.4(e)	PEC Performance of PbS/ZnO NRAs	190
5.4	Results and Discussions of In ₂ S ₃ /PbS/ZnO NRAs.....	192
5.4.1	Effect of SILAR Cycles	195
5.4.1(a)	Structural Analysis	195
5.4.1(b)	Morphological Study	196
5.4.1(c)	Optical Analysis	198
5.4.1(d)	PEC Performance of In ₂ S ₃ /PbS/ZnO NRAs.....	200
5.4.2	Effect of Dipping Time	202
5.4.2(a)	Structural Analysis	202
5.4.2(b)	XPS Analysis of In ₂ S ₃ /PbS/ZnO NRAs Surface	205
5.4.2(c)	Morphological Study	207
5.4.2(d)	Optical analysis.....	209
5.4.2(e)	PEC Performance of In ₂ S ₃ /PbS/ZnO NRAs.....	210
CHAPTER 6 CONCLUSION AND FUTURE RECOMMENDATIONS ..		213
6.1	Conclusion.....	213
6.2	Recommendations for Future Investigations.....	216
REFERENCES.....		217
APPENDICES		
LIST OF PUBLICATIONS		
INTERNATIONAL CONFERENCES		

LIST OF TABLES

		Page
Table 2.1	Quantum confined structure classification.....	22
Table 2.2	Overview on In ₂ S ₃ /ZnO and PbS/ZnO thin films used for photoelectrochemical cells.....	68
Table 3.1	Chemical substances, materials, and solvents used in this work.	73
Table 3.2	Parameters studied in In ₂ S ₃ /ZnO/ ITO via SILAR method.	78
Table 3.3	Parameters studied in PbS/ZnO/ ITO via SILAR method.	78
Table 3.4	Parameters studied in In ₂ S ₃ /PbS/ZnO NRAs/ITO.	79
Table 3.5	Compounds and their JCPDS reference codes.....	83
Table 4.1	A overview of the morphological, optical, and PEC properties of ZnO NPs deposited via RF sputtering as a role of the thermal temperature.	107
Table 4.2	A overview of the morphological, optical, and PEC properties of ZnO NPs deposited via sol-gel spin coating as a role of the thermal temperature.	116
Table 4.3	Atomic% of Zn and O in the ZnO NRAs obtained from EDX spectral analyses.....	123
Table 4.4	A overview of the morphological, optical, and PEC properties of ZnO NRs synthesized via the hydrothermal method as a result of growth times.....	132
Table 4.5	Photoelectrochemical water-splitting cell performance of the proposed optimum ZnO NRAs-8h as photoanode when compared with other reports in the literature.....	134
Table 5.1	SILAR cycles deposition-dependent Energy gap, J_{ph} and the percentage photoconversion efficiencies (η) of the deposited In ₂ S ₃ /ZnO NRAs.	146
Table 5.2	FTIR data for the ZnO NRs, and In ₂ S ₃ /ZnO NRAs- 300°C.	157
Table 5.3	EDS data for the In In ₂ S ₃ /ZnO core-shell NRAs- 300°C.....	163

Table 5.4	A overview of the optimum electrode, optical, and PEC Performance of the $\text{In}_2\text{S}_3/\text{ZnO}$ NRAs synthesized in various experimental parameters.	167
Table 5.5	The photoelectrochemical conversion efficiency of PbS/ZnO NRAs/ITO at different dipping time.	179
Table 5.6	The photoelectrochemical conversion efficiency of PbS/ZnO NRAs/ITO at different cationic concentration.	183
Table 5.7	A overview of the optimum electrode, optical, and PEC Performance of the PbS/ZnO NRAs synthesized in various experimental parameters.	192
Table 5.8	EDS data for the $\text{In}_2\text{S}_3/\text{PbS}/\text{ZnO}$ heterostructure NRAs-18s.	209
Table 5.9	A overview of the optimum electrode, optical, and PEC Performance of the $\text{In}_2\text{S}_3/\text{PbS}/\text{ZnO}$ NRAs synthesized in various experimental parameters.	212

LIST OF FIGURES

		Page
Figure 2.1	A diagram depicting the heterostructured-alignment process, with C.B. and V.B. representing the valence and conduction bands, respectively. (a) Type I band alignment, "straddling," (b) Type II staggered gap, and (c) Type III broken gap	14
Figure 2.2	Energy band diagram for a n-type semiconductor	19
Figure 2.3	Quantum confinement of 0D, 1D, 2D, and 3D nanostructures with density of states (DOS) effects.....	23
Figure 2.4	A demonstration of three different ZnO crystal structures: (a) cubic rock salt, (b) cubic zinc blend, and (c) hexagonal wurtzite structure [86, 87].....	25
Figure 2.5	Wurtzite crystal structure of zinc oxide with a hexagonal unit cell and different of crystallographic facets [88]	26
Figure 2.6	Diagram of the approaches used to synthesise ZnO thin films.....	27
Figure 2.7	Schematic of an RF magnetron sputtering system [95]	28
Figure 2.8	Sol-gel coating Thin-film deposition techniques: a) spin-coating and b) dip-coating [101].....	30
Figure 2.9	Schematic diagram deposition SILAR growth. (i) adsorption of precursor KL_p on the substrate surface and the formation of the electrical double layer; (ii) rinsing step; (iii) reaction of KL_p surface species with the precursor AL'_q and (iv) rinsing(II)	43
Figure 2.10	Schematic of tetragonal crystal structure of In_2S_3 , Indium is shown in red, while sulfur atoms are depicted in blue [153].....	46
Figure 2.11	Schematic of PbS cubic crystal structure	59
Figure 3.1	Research flowchart schematic diagram.....	72
Figure 3.2	Schematic diagram of the fabrication of a ZnO NPs seed layer using sol-gel spin coating.....	75
Figure 3.3	Schematic diagram of the hydrothermal method of synthesised ZnO NRAs	76

Figure 3.4	Diagram of the SILAR method for the preparation of In ₂ S ₃ /ZnO NRAs, Xdip-MV1 Apex Multi Vessel SILAR Coating instrument, and Tube furnace.....	77
Figure 3.5	The schematic diagram of X-ray diffraction[189]	83
Figure 3.6	Schematic of an FTIR spectrometer [190].....	84
Figure 3.7	Schematic illustration of Field Emission Scanning Electron Microscope [193]	86
Figure 3.8	Transmission Electron Microscope and the main components [194]	89
Figure 3.9	Principle of Fluorescence spectroscopy (Photoluminescence) [195]	90
Figure 3.10	Schematic representation of the principle of XPS	91
Figure 3.11	Set-up for photoelectrochemical experiments [200].....	95
Figure 4.1	XRD patterns of ZnO NPs annealed at various temperatures 250, 300, 350, 400 and 450 °C	98
Figure 4.2	FESEM micrographs (magnification of ×300000) of the seed layer annealed at various temperatures (a) 250, (b) 300, (c) 350, (d) 400, (e) 450 °C and (f)The particle and crystal sizes vs annealing temperature.....	100
Figure 4.3	EDX results of the proposed ZnO NPs annealed at various temperatures (a) 250, (b) 300, (c) 350, (d) 400 and (e) 450 °C.....	102
Figure 4.4	Absorption spectra of ZnO NPs are annealed at various temperatures 250, 300, 350, 400 and 450 °C	103
Figure 4.5	Optical band gap energies evaluation of ZnO NPs annealed at various temperatures 250, 300, 350, 400 and 450 °C	104
Figure 4.6	Linear sweep voltammograms of the optimum ZnO NPs annealed at various temperatures (a) 250, (b) 300, (c) 350, (d) 400 and 450 °C.....	105
Figure 4.7	FESEM micrographs of the seed layer ZnO NPs annealed at various temperatures (a) 300, (b) 350, (c) 400, (d) 450 °C	108
Figure 4.8	X-ray diffractogram of ZnO NPs annealed at different temperatures: (a) plain ITO;(b) 300; (c) 350; (d) 400; and(e) 450°C	110
Figure 4.9	FTIR spectrum of ZnO nanoparticles annealed at 400°C	110

Figure 4.10	The absorbance spectra of ZnO NPs annealed at the different temperatures: (a) 300; (b) 350; (c) 400; and (d) 450 °C.....	111
Figure 4.11	Bandgap energy curves of ZnO NPs annealed at the different temperatures: (a) 300; (b) 350; (c) 400; and (d) 450 °C.....	113
Figure 4.12	UV PL spectra of ZnO NPs annealed at the different temperatures: (a) 300; (b) 350; (c) 400; and (d) 450 °C	114
Figure 4.13	Linear sweep voltammograms of ZnO/ITO NPs annealed at the different temperatures (a) 300; (b) 350; (c) 400; (d) 450 °C.....	115
Figure 4.14	XRD profiles of ITO and ZnO NRAs made at various hydrothermal growth times	118
Figure 4.15	FTIR spectrum of ZnO NRAs prepared at various hydrothermal growth times.....	119
Figure 4.16	FE-SEM images (top view) of ZnO NRAs prepared at various hydrothermal growth times: (a) 4; (b) 6; (c) 8; (d) 10;and (e) 12h ..	121
Figure 4.17	EDX spectra of ZnO NRAs prepared at various hydrothermal growth times with indicated scanned area in the FE-SEM image ...	122
Figure 4.18	(a-b) TEM images, (c) HRTEM images, (d) EDX spectra of the ZnO NRAs-8h (Inset: EDX analyses for elemental composition) and (e-g) EDX maps.....	124
Figure 4.19	PL spectra of ZnO NRAs prepared at various hydrothermal growth times	126
Figure 4.20	(a) The absorbance spectra and (b) Tauc plot $(\alpha h\nu)^2$ versus energy $(h\nu)$ of ZnO NRAs prepared at various hydrothermal growth times	127
Figure 4.21	Hydrothermal growth times-dependent variation in the E_g values of ZnO NRAs	128
Figure 4.22	(a) Survey spectrum and (b) High resolution XPS spectrum of O 1s and (c) Zn 2p of ZnO NRAs-8h.....	129
Figure 4.23	LSV response of ZnO NPs (seed layer) and ZnO NRAs prepared at various growth times	130
Figure 4.24	Values of $\eta\%$ for ZnO NPs and ZnO NRAs obtained at various hydrothermal growth times	131
Figure 5.1	XRD patterns of the (a) ZnO NRAs and In ₂ S ₃ /ZnO prepared by adopting different SILAR cycles: (b) 2; (c) 4; (d) 6; (e) 8; (f) 10	

	cycles. The inset of figure represents the peaks plotted from 30° to 36°	137
Figure 5.2	FESEM images (top view) of (a) bare ZnO NRs and In ₂ S ₃ /ZnO;(b-f) 2-10 cycles; (g) EDX (In ₂ S ₃ /ZnO-6cy); (h) NRAs diameter.....	139
Figure 5.3	(a) UV–Vis spectra and (b) $(ah\nu)^2$ versus photon energy of pure ZnO NRAs and In ₂ S ₃ /ZnO NRAs prepared by adopting different SILAR cycles	141
Figure 5.4	Room temperature PL spectra: (a) bare ZnO NRAs and (b-f) In ₂ S ₃ /ZnO core-shell heterostructure NRAs	143
Figure 5.5	Linear sweep voltammograms obtained for: bare ZnO NRAs/ITO; In ₂ S ₃ /ZnO NRAs prepared by different SILAR cycles (2, 4, 6, 8 and 10 cycles).....	145
Figure 5.6	Photoconversion efficiency (η) values as a function of applied voltage versus Ag/AgCl of ZnO NPs; ZnO NRAs; In ₂ S ₃ /ZnO NRAs prepared at different SILAR cycles (2, 4, 6, 8 and 10 cycles)	146
Figure 5.7	X-ray diffraction of: (a) ZnO NRAs; In ₂ S ₃ /ZnO NRAs/ITO at different dipping time of (b) 6; (c) 12; (d) 18; (e) 24; and (f) 30s ...	147
Figure 5.8	(a) UV-Vis Spectra; (b) bandgap energy curves of ZnO NRAs/ITO and In ₂ S ₃ /ZnO NRAs/ITO prepared at different dipping times of 6; 12;18; 24; and 30s	148
Figure 5.9	Linear sweep voltammograms obtained for: bare ZnO NRAs/ITO; In ₂ S ₃ /ZnO NRAs/ITO at different dipping time 6; 12; 18; 24; and 30s	150
Figure 5.10	Photoconversion efficiency as a function of applied voltage versus (Ag/AgCl) of ZnO NPs; ZnO NRAs; In ₂ S ₃ /ZnO NRAs prepared with different dipping time: 6; 12; 18; 24; and 30s.....	151
Figure 5.11	X-ray diffraction of: (a) ZnO NRAs; In ₂ S ₃ /ZnO NRAs/ITO at different cationic concentration of (b) 0.0005; (c) 0.001; (d) 0.002; (e) 0.003; and (f) 0.03M. The inset of figure represents the peaks plotted from 30° to 36°	152
Figure 5.12	(a) UV-Vis Spectra; (b) bandgap energy curves of: ZnO NRAs and In ₂ S ₃ /ZnO NRAs prepared at different cationic concentration: 0.0005; 0.001; 0.002; 0.003; and 0.03M.....	153

Figure 5.13	Linear sweep voltammograms obtained for bare ZnO NRAs; In ₂ S ₃ /ZnO NRAs at different cationic concentration: 0.0005; 0.001; 0.002; 0.003; and 0.03M	154
Figure 5.14	Photoconversion efficiency as a function of applied voltage versus (Ag/AgCl) of ZnO NPs; ZnO NRAs; In ₂ S ₃ /ZnO NRAs prepared with different cationic concentration: 0.0005; 0.001; 0.002; 0.003; and 0.03M	155
Figure 5.15	X-ray diffraction of: (a) ZnO NRAs; In ₂ S ₃ /ZnO NRAs at different annealing temperature of (b) 100; (c) 200; (d) 300; (e) 400; and (f) 500°C. The inset of figure represents the peaks plotted from 24° to 36°	156
Figure 5.16	FTIR of (a) ZnO NRAs, and (b) In ₂ S ₃ /ZnO NRAs-300°C	157
Figure 5.17	XPS spectra of (a) In ₂ S ₃ /ZnO core-shell heterostructure NRAs; (b) Zn 2p; (c) O 1s; (d) S 2p; (e) In 3d	159
Figure 5.18	FESEM images of the top view of (a) bare ZnO NRAs (b) In ₂ S ₃ /ZnO core-shell heterostructure NRAs (300°C)	161
Figure 5.19	TEM (a), HRTEM images (b,c) and EDS spectrum (d,e) of the In ₂ S ₃ /ZnO heterostructures- 300°C.....	163
Figure 5.20	(a) UV-Vis Spectra; (b) bandgap energy curves of: ZnO NRAs and In ₂ S ₃ /ZnO NRAs prepared at different at different annealing temperature of 100; 200; 300; 400; and 500°C.....	164
Figure 5.21	Linear sweep voltammograms obtained for: bare ZnO NRAs; In ₂ S ₃ /ZnO NRAs at different annealing temperature: 100; 200; 300; 400; and 500°C	166
Figure 5.22	Photoconversion efficiency as a function of applied voltage versus (Ag/AgCl) of ZnO NPs; ZnO NRAs; In ₂ S ₃ /ZnO NRAs prepared with different annealing temperature: 100; 200; 300; 400; and 500°C	167
Figure 5.23	X-ray diffractogram of: (a) bare ZnO NRAs; PbS/ZnO NRAs prepared at different SILAR cycles: (b) 3; (c) 5; (d) 7; (e) 9; and (f) 11 cycles. The inset of figure represents the peaks plotted from 30° to 36°	169

Figure 5.24	FESEM images (top view) of (a) bare ZnO NRs and PbS/ZnO;(b-f) 3-11 cycles; (g) EDX (PbS/ZnO NRAs- 7Cy); (h) Diameters of nanorods	171
Figure 5.25	(a) UV-Vis Spectra; (b) the optical bandgap energy curves of: ZnO NRAs; PbS/ZnO NRAs prepared at different SILAR cycles: 3; 5; 7; 9; and 11 cycles.....	172
Figure 5.26	Room temperature PL spectra: (a) bare ZnO NRAs and (b-f) PbS/ZnO heterostructure NRAs at different SILAR cycles.....	173
Figure 5.27	Linear sweep voltammograms obtained for: bare ZnO NRAs; PbS/ZnO NRAs/ITO prepared at different SILAR cycles: 3; 5; 7; 9; and 11 cycles.....	174
Figure 5.28	Photoconversion efficiency values as a function of applied voltage vs. Ag/AgCl of ZnO NPs; ZnO NRAs; PbS/ ZnO NRAs at different SILAR cycles: 3; 5; 7; 9; and 11 cycles	175
Figure 5.29	X-ray diffractogram of: (a) bare ZnO NRAs; PbS/ZnO NRAs/ITO prepared at SILAR dipping time: (b) 24; (c) 36; (d) 48; (e) 60; and (f) 72s. The inset of figure represents the peaks plotted from 30° to 36°	176
Figure 5.30	(a) UV-Vis Spectra; (b) the optical bandgap energy curves of: ZnO NRAs; PbS/ZnO NRAs prepared at different dipping time: 24; 36; 48; 60; and 72s	177
Figure 5.31	Linear sweep voltammograms obtained for: bare ZnO NRAs; PbS/ZnO NRAs prepared at different dipping time: 24; 36; 48; 60; and 72s	178
Figure 5.32	X-ray diffractogram of: (a) bare ZnO NRAs; PbS/ZnO NRAs prepared at different SILAR cationic concentration: (b) 0.001; (c) 0.002; (d) 0.003; (e) 0.004; and (f) 0.005M. The inset of figure represents the peaks plotted from 30° to 36°	180
Figure 5.33	(a) UV-Vis Spectra; (b) the optical bandgap energy curves of: ZnO NRAs; PbS/ZnO NRAs prepared at different SILAR cationic concentration: 0.001; 0.002; 0.003; 0.004; and 0.005M	181
Figure 5.34	Linear sweep voltammograms obtained for: bare ZnO NRAs; PbS/ZnO NRAs prepared at different SILAR cationic concentration: 0.001; 0.002; 0.003; 0.004; and 0.005M	182

Figure 5.35	X-ray diffractogram of: (a) bare ZnO NRAs; PbS/ZnO NRAs/ITO prepared at different annealing temperature: (b) 100; (c) 200; (d) 300; (e) 400; and (f) 500 °C. The inset of figure represents the peaks plotted from 30° to 36°	184
Figure 5.36	FTIR of (a) ZnO NRAs, and (b) PbS/ZnO heterostructure NRAs-200 °C.....	184
Figure 5.37	(a) XPS survey spectrum of PbS/ZnO, (b) High resolution core level XPS spectrum of Zn2p, (c) High resolution core level XPS spectrum of O1s, (d) high resolution core level XPS spectrum of Pb4f, (e) high resolution core level XPS spectrum of S2p	187
Figure 5.38	The TEM (a-c), HRTEM (d) and EDX (e,f) of PbS/ZnO-200 °C ...	189
Figure 5.39	(a) UV-Vis Spectra; (b) the optical bandgap energy curves of: ZnO NRAs; PbS/ZnO NRAs prepared at different annealing temperature: 100; 200; 300; 400; and 500 °C	190
Figure 5.40	Linear sweep voltammograms obtained for: bare ZnO NRAs; PbS/ZnO NRAs prepared at different annealing temperature: 100; 200; 300; 400; and 500 °C.....	191
Figure 5.41	Photoconversion efficiency values as a function of applied voltage vs. Ag/AgCl of ZnO NPs; ZnO NRAs; PbS/ ZnO NRAs at different annealing temperature: 100; 200; 300; 400; and 500 °C.....	192
Figure 5.42	Diagram of Schematic of the relative energy levels and ideal cascade band structure in In ₂ S ₃ /PbS /ZnO NRAs/ITO heterostructure ternary system	193
Figure 5.43	X-ray diffractogram of: (a) bare ZnO NRAs; In ₂ S ₃ /PbS/ZnO NRAs prepared at different SILAR cycles: (b) 2; (c) 4; (d) 6; (e) 8; and (f) 10 cycles. The inset of figure represents the peaks plotted from 30° to 44°	196
Figure 5.44	FESEM images (top view) of (a) bare ZnO NRs and In ₂ S ₃ /PbS/ZnO;(b-f) 2-10 cycles; (g) EDX(In ₂ S ₃ /PbS/ZnO NRAs-8Cy); (h) Diameters of nanorods	197
Figure 5.45	(a) UV-Vis Spectra; (b) the optical bandgap energy curves of: ZnO NRAs; In ₂ S ₃ /PbS/ZnO NRAs prepared at different SILAR cycles: 2; 4; 6; 8; and 10 cycles.....	199

Figure 5.46	Room temperature PL spectra: (a) bare ZnO NRAs and (b-f) $\text{In}_2\text{S}_3/\text{PbS}/\text{ZnO}$ heterostructure NRAs	200
Figure 5.47	Linear sweep voltammograms obtained for: bare ZnO NRAs; PbS/ZnO NRAs and $\text{In}_2\text{S}_3/\text{PbS}/\text{ZnO}$ NRAs prepared at different SILAR cycles: 2; 4; 6; 8 and 10 cycles	201
Figure 5.48	Photoconversion efficiency values as a function of applied voltage vs. Ag/AgCl of ZnO NPs; ZnO NRAs; PbS/ZnO NRAs; $\text{In}_2\text{S}_3/\text{PbS}/\text{ZnO}$ NRAs at different SILAR cycles: 2; 4; 6; 8; and 10 cycles.....	202
Figure 5.49	X-ray diffractogram of: (a) bare ZnO NRAs; $\text{In}_2\text{S}_3/\text{PbS}/\text{ZnO}$ NRAs prepared at different SILAR dipping time: (b) 12; (c) 18; (d) 24; (e) 30; and (f) 36s. The inset of figure represents the peaks plotted from 30° to 37°	204
Figure 5.50	FTIR of (a) ZnO NRAs, and (b) $\text{In}_2\text{S}_3/\text{PbS}/\text{ZnO}$ heterostructure NRAs-18s.....	205
Figure 5.51	(a) XPS survey spectrum of $\text{In}_2\text{S}_3/\text{PbS}/\text{ZnO}$, (b) High resolution core level XPS spectrum of Zn2p, (c) O1s, (d) Pb4f, (e) S2p,(f) In3d	207
Figure 5.52	(a, b, c, d) TEM images; (e) HRTEM image (f) TEM elemental mapping; and (g) EDX of $\text{In}_2\text{S}_3/\text{PbS}/\text{ZnO}$ heterojunction-18s	208
Figure 5.53	(a) UV-Vis Spectra; (b) the optical bandgap energy curves of: ZnO NRAs/ITO; $\text{In}_2\text{S}_3/\text{PbS}/\text{ZnO}$ NRAs/ITO prepared at different SILAR dipping times: 12; 18; 24; 30; and 36s	209
Figure 5.54	Linear sweep voltammograms obtained for: bare ZnO NRAs; PbS/ZnO NRAs/ITO and $\text{In}_2\text{S}_3/\text{PbS}/\text{ZnO}$ NRAs/ITO prepared at different SILAR dipping times: 12; 18; 24; 30; and 36s.....	210
Figure 5.55	Photoconversion efficiency values as a function of applied voltage vs. Ag/AgCl of ZnO NPs; ZnO NRAs; PbS/ZnO NRAs; and $\text{In}_2\text{S}_3/\text{PbS}/\text{ZnO}$ NRAs at different SILAR dipping times: (a) 12; (b) 18; (c) 24; (d) 30; and (f) 36s	211

LIST OF SYMBOLS

\AA	Angstrom
D	Average crystallite size
d_{hkl}	Inter-plane distance between the two neighboring lattice planes
E	Energy
E_g	Band gap
h	Planck's constant
$h\nu$	Energy of photon
I	Current
K	Kelvin
k	Boltzmann's constant
n	Nature of the electronic transition
$^{\circ}\text{C}$	Celsius
T	Temperature
V	Volt
α	Absorption coefficient
β	Full width at half maximum (FWHM)
θ	Bragg's angle
λ	Wavelength
J_{ph}	Photocurrent density
V_{app}	Voltage applied
J_{sc}	Short-circuit current density
V_{oc}	Open-circuit voltage

LIST OF ABBREVIATIONS

C.B	Conduction band
CE	Counter electrode
DDW	Double distilled water
DEA	Diethanolamine
EDS	Energy Dispersive X-Ray Spectroscopy
EMA	Effective Mass Approximation
FESEM	Field Emission Scanning Electron Microscopy
FTIR	Fourier-transform infrared spectroscopy
FWHM	Full width at half maximum
HMTA	Hexamethylenetetramine
HRTEM	High Resolution-Transmission Electron Microscopy
ITO	Indium Tin Oxide
LSV	Linear Sweep Voltammetry
NPs	Nanoparticle
NRA _s	Nanorods Arrays
NR _s	Nanorods
OH	Hydroxyl
<i>Ox.</i>	Oxidation
PEC	Photoelectrochemical
<i>Red.</i>	Reduction
RE	Reference electrode
SILAR	Successive ion layer adsorption and reaction
TEM	Transmission Electron Microscopy
UV-Vis	Ultraviolet-visible
V.B	Valence band
WE	Working electrode
XRD	X-ray diffraction
ZnO	Zinc oxide

LIST OF APPENDICES

APPENDIX A	INDIUM TIN OXIDE XRD DATABASE
APPENDIX B	ZINC OXIDE XRD DATABASE
APPENDIX C	INDIUM SULFIDE XRD DATABASE
APPENDIX D	LEAD SULFIDE XRD DATABASE

**SINTESIS DAN PENCIRIAN ZINK OKSIDA NANOROD DIPEKA
OLEH In_2S_3 , PBS DAN In_2S_3 -PBS UNTUK APLIKASI
FOTOELEKTROKIMIA**

ABSTRAK

Kajian ini memberi tumpuan kepada sintesis dan pencirian zink oksida yang nanorod dipeka oleh logam kalkogenida jurang tenaga sempit untuk aplikasi fotoelektrokimia. Dalam kajian ini, lapisan benih nanozarah ZnO (NPs) telah disediakan melalui teknik salutan percikan RF Magnetron dan sol-gel berputar diikuti dengan rawatan haba pada suhu berbeza untuk mengoptimumkan nukleasi. Barisan rod nano ZnO kemudiannya ditumbuhkan melalui kaedah hidroterma yang mudah dan ringkas. Kesan suhu dan tempoh pertumbuhan hidroterma dioptimumkan untuk mendapatkan nisbah aspek ZnO NRAs yang tinggi. $\text{In}_2\text{S}_3/\text{ZnO}$ NRAs/ITO, PbS/ZnO NRAs /ITO telah disediakan menggunakan kaedah penjerapan dan tindak balas lapisan ionik berturut (SILAR). Sebagai tambahan, dengan mengandaikan kesan pelbagai parameter ke atas pembentukan komposit nano $\text{In}_2\text{S}_3/\text{ZnO}$ dan PbS/ZnO NRAs /ITO, sintesis telah dijalankan dengan variasi bilangan kitaran SILAR, masa pencelupan, kepekatan prekursor kationik dan suhu penyepuhlindapan. Pembentukan rod nano ZnO dan In_2S_3 dapat dikesan apabila warna sampel berubah daripada tidak berwarna kepada putih untuk ZnO, dan coklat gelap untuk $\text{In}_2\text{S}_3/\text{ZnO}$. Analisis pembelauan X-ray (XRD) mengesahkan bahawa sampel ZnO NRAs yang disintesis mempunyai fasa heksagonal manakala In_2S_3 mempunyai struktur kristal tetrahedral. Pemeka tenaga cahaya yang dikenakan tidak memberi kesan terhadap struktur bahan hos. Struktur kecil kulit In_2S_3 pada ZnO NRA telah diperhatikan melalui mikroskop elektron penghantaran (TEM). Sementara itu, mikroskopi transmisi elektron (SEM) memberi

anggaran purata saiz cangkerang $\text{In}_2\text{S}_3/\text{ZnO}$ heterostruktur diikuti penentuan jarak pinggiran kekisi (d-spacing) daripada mikroskopi transmisi elektron beresolusi tinggi (HR-TEM). Komposit nano $\text{In}_2\text{S}_3/\text{ZnO}$ NRA yang disintesis pada keadaan optimum memberikan ketumpatan arus tenaga cahaya maksimum pada 1.301 mA/cm^2 dan kecekapan penukaran tenaga cahaya sebanyak 0.95% iaitu dua kali lebih baik daripada ZnO NRAs kosong (0.46%). Gabungan semikonduktor ZnO berluang tenaga luas dengan semikonduktor berluang tenaga sempit telah menghasilkan lenturan posisi aras Fermi yang berlainan. Oleh itu, elektron terjana tenaga cahaya dapat dipindahkan dengan mudah daripada jalur konduksi In_2S_3 ke jalur konduksi ZnO sementara lohong dipindahkan dari jalur valensi ZnO NRAs ke jalur valensi In_2S_3 . Seterusnya, pembentukan nanorod ZnO dan PbS diperhatikan apabila warna sampel berubah daripada tidak berwarna kepada putih untuk ZnO NRAs dan warna coklat gelap untuk sampel PbS/ZnO . Komposit nano PbS/ZnO NRA yang disintesis pada keadaan optimum memberikan ketumpatan arus tenaga cahaya maksimum pada 4.30 mA/cm^2 dan kecekapan penukaran tenaga cahaya sebanyak 3.14% iaitu tujuh kali lebih baik daripada ZnO NRAs kosong (0.46%). Sebagai tambahan, filem nipis komposit nano ternari $\text{In}_2\text{S}_3/\text{PbS}/\text{ZnO}$ NRAs telah dioptimumkan melalui kawalan bilangan kitaran SILAR dan masa pencelupan. Komposit nano $\text{In}_2\text{S}_3/\text{PbS}/\text{ZnO}$ NRA yang disintesis pada keadaan optimum memberikan ketumpatan arus tenaga cahaya maksimum pada 7.76 mA/cm^2 dan kecekapan penukaran tenaga cahaya sebanyak 5.70% iaitu 12.4 kali lebih baik daripada ZnO NRAs kosong (0.46%). Keputusan mendapati jurang tenaga yang sempit menyebabkan sampel yang diaplikasikan In_2S_3 dan PbS dapat menyerap lebih banyak cahaya berbanding dengan ZnO NRAs kosong. Sebagai perbandingan dengan elektrod PEC ZnO NRAs/ITO berluang tenaga 3.23 eV, $\text{In}_2\text{S}_3/\text{ZnO}/\text{ITO}$ dan $\text{PbS}/\text{ZnO}/\text{ITO}$ menunjukkan jurang tenaga yang lebih kecil iaitu masing-masing 2.27

eV dan 2.73 eV. Penurunan berlata jurang jalur ini mengurangkan peluang untuk penggabungan semula elektron-lubang dan meningkatkan kecekapan pengumpulan elektron.

**SYNTHESIS AND CHARACTERISATION OF ZINC OXIDE
NANORODS SENSITISED BY In_2S_3 , PBS AND In_2S_3 -PBS FOR
PHOTOELECTROCHEMICAL APPLICATION**

ABSTRACT

This study focuses on the synthesis and characterisation of zinc oxide nanorods sensitised by narrow bandgap energy metal chalcogenides for photoelectrochemical application. In this study, ZnO nanoparticles seed layer (NPs) was prepared by RF Magnetron sputtering and sol-gel spin coating technique, followed by heat-treatment at different temperatures to optimise the nucleation. ZnO nanorod arrays (NRAs) were then grown through a simple, facile hydrothermal method on the optimised seed layer sample. The effect of hydrothermal growth duration was optimised to ensure achieving the high aspect ratio of ZnO NRAs. $\text{In}_2\text{S}_3/\text{ZnO}$ NRAs/ITO and PbS/ZnO NRAs/ITO were prepared using successive ionic layer adsorption and reaction (SILAR) method. In addition, considering the effect of various parameters on formation of $\text{In}_2\text{S}_3/\text{ZnO}$ NRAs and PbS/ZnO NRAs nanocomposite, the synthesis was carried out with variation in number of SILAR cycles, dipping time, concentration of cationic precursor, and annealing temperature. The formation of ZnO nanorods and In_2S_3 was noticed when the colour of the samples changed from colourless to white for ZnO, and yellow for $\text{In}_2\text{S}_3/\text{ZnO}$. The powder X-ray diffraction (XRD) analysis verified that the synthesised ZnO NRAs sample has hexagonal phase, whereas In_2S_3 has tetrahedral crystal structure. The deposited photosensitiser has no effect on the host material structure. The nanocomposite shell of In_2S_3 on ZnO NRAs was observed by Transmission Electron Microscopes (TEM). TEM provided the estimated average shell width size of the $\text{In}_2\text{S}_3/\text{ZnO}$ heterostructure, followed by determination of lattice

fringe (d-spacing) from high-resolution transmission electron microscopy (HR-TEM). In₂S₃/ZnO NRAs nanocomposite synthesised at optimum condition provided a maximum photocurrent density of 1.301 mA/cm² and photoconversion efficiency of 0.95%, which was two times greater than the plain ZnO NRAs (0.46%). The combination of wide bandgap energy (ZnO) with narrow bandgap energy semiconductor caused bending of different Fermi-level positions. Thus, the photogenerated electrons can be transferred easily from conduction band of In₂S₃ to the conduction band of ZnO, while the holes transferred from the valence band of ZnO NRAs to the valence band of In₂S₃. Furthermore, the formation of ZnO NRAs and PbS was observed as the colour of the samples changed from colourless to white for ZnO NRAs and dark brown for the PbS/ZnO sample. PbS/ZnO NRAs nanocomposite synthesised at optimum condition exhibited a maximum photocurrent density of 4.30 mA/cm² and photoconversion efficiency of 3.14%, which was found to be around seven times greater than the plain ZnO NRAs (0.46%). Additionally, ternary nanocomposite thin film In₂S₃/PbS/ZnO NRAs has been optimised via controlling SILAR cycle number and dipping time. In₂S₃/PbS/ZnO NRAs nanocomposite synthesised at optimum condition exhibited a maximum photocurrent density of 7.76 mA/cm² and photoconversion efficiency of 5.70%, which was found to be around 12.4 times greater than the plain ZnO NRAs (0.46%). Results showed that due to its narrow bandgap, In₂S₃ and PbS deposited samples were able to harvest more light compared to plain ZnO NRAs. In comparison with ZnO NRAs/ITO PEC electrode with a bandgap of 3.23 eV, In₂S₃/ZnO /ITO and PbS/ZnO/ITO demonstrated much smaller bandgaps of 2.27 eV, 2.73 eV, respectively. This cascading bands gap alignment decreased the chance for electron-hole recombination and enhanced the efficiency of electrons collection.

CHAPTER 1

INTRODUCTION

1.1 Background of the Study

In order to meet the world's enormous energy demand, it is imperative that we concentrate our efforts to identify the resources and supply of energy that can be used to replace fossil fuels. Carbon fuel combustion results in catastrophic climate change due to increased in the concentration of carbon dioxide and monoxide because of the increased use of fossil fuels [1]. In order to replace fossil fuels by the turn of the century, renewable energy resources should be taken into account. For example, geothermal and tidal power, wind power, solar energy, biofuel, and hydropower can be a potential replacements. As the amount of energy consumed almost exactly corresponds to the economic growth rate in addition to private contentment, it is obvious that humankind's ability to continue developing at its current rate will be dependent on the availability of appropriate and sufficient energy. To avoid further environmental catastrophe, it is necessary to develop less expensive and pollution-free energy sources, which could be obtained by sun energy harvesting. Solar-based energy is the most appealing and abundant option, with the potential to supply 10000 times the consumed total annual energy. Furthermore, it has no effect on the stabilization of heat energy on our planet and would not result in contamination of any kind of our environment [2,3].

Although solar energy is abundant, the main impediment to its widespread use is the high costs associated with it, as well as the low conversion capability of currently available photo converters. Fossil fuels are a concentrated energy source, whereas the sun provides photons with a moderate power density that is distributed in a relatively consistent manner across the entire planet. Many different approaches to harness solar

energy have been developed up to this point [4]. The visible light spectrum has been efficiently utilised by a number of technologies, including photovoltaic [5], photochemical, photoelectrochemical, and photothermal cells [5,6]. In the field of photoelectrochemical conversion, a number of review articles [7–9] have recently been published. Several tries conducted with separate solar conversion systems over the past two to three decades. Photoelectrochemistry was born as a result of the development of photovoltaic devices, which allowed for the establishment of a connection between photovoltaic devices and electrochemical devices. To further strengthen the field, subsequent developments, e.g., photoelectrochemical solar cells (PECs), were utilized [10]. Among the methods listed above, photoelectrochemical cells have recently gained popularity as a low-cost method of converting sun energy converted to chemical energy. After that, large conversion efficiency of electrical energies was also popular and at the same time they maintain the low cost. Furthermore, there is a continued search for cost-effective materials for photoelectrodes. Numerous efforts have been undertaken to enhance photoanode material performance while preserving or improving its overall quality. The study of semiconductor nanomaterials, which can be used as a photoanode in photoelectrochemical cells, is currently gaining momentum and is expected to continue to grow. Moreover, metal oxide semiconductor nanomaterials have gained in popularity due to their outstanding structural flexibility as well as a variety of additional attractive features [11].

In addition to exhibiting desirable properties because of their bulk, e.g., photodetection, chemical sensing, and photoelectrochemical efficiency, metal oxide nanostructures also exhibit properties related to their size confinement and highly anisotropic geometry [12]. The research of nanostructures of novel metal oxides is a quietly stunning topic and development both from a fundamental and a secondary

perspective and a broad perspective. The reasons behind that are the composites combining unique and established characteristics that have distinct influence of nanostructure. Zinc oxide (ZnO) had gained critical appreciation of the various oxides of metals due to its distinguishing characteristics, which include its ease of low-temperature crystallisation, high mobility of electrons and large range of applications in optoelectronics. Specifically, nanostructures of ZnO are of particular interest due to their synthesizable in a variety of morphologies using a variety of different methods [13]. Multiple ways exist for synthesizing ZnO nanostructures, in addition to sensitising Zinc Oxide, have been developed over the course of several decades of research. The successive ionic layer adsorption and reaction (SILAR) method, hydrothermal technique, RF Magnetron sputtering and the sol-gel spin coating technique are four of the most widely used methods [14, 15].

Due to its vast surface area, the structure of ZnO Nanorod Arrays (NRAs) in one dimension has been thoroughly explored, particularly when compared to other diversified nanostructural structures. With respect to PEC applications, an expanse of area of the surface is the most important aspect in obtaining maximum effectiveness [16]. In 1935, ZnO characteristic, as an example its energy with a broad band gap 3.37 eV, excitation energy that is large (60 meV) and $300 \text{ cm}^2 \text{ V}^{-1} \cdot \text{s}^{-1}$ electronic mobility at its height first gained the popularity in community of researchers. These properties were particularly useful in the sectors of application for optoelectronic energy with a short wavelength. Regardless of its numerous advantages over ZnO NRAs as a semiconductor with a large and direct band gaps, owing to the unavailability of visible light harvesting, ZnO's applicability in optoelectronics are limited [17]. As a result, modifications to ZnO NRAs should be made to boost the harvesting of absorption in the visible light spectrum. This can be performed by sensitizing the surface in order to

modify the energy band gap, which is relatively large. Diverse approaches, such as organic dye doping [18], synthesising heterostructures [9], dye sensitisation [19] and sensitivity via the use of small bandgap energy chalcogenide materials has proved successful [20]. Energy with a narrow band gap of the metal chalcogenide semiconductors have been chosen from amid the aforementioned techniques because of their high coefficient of absorption, great degree of steadiness, bandgap that is adaptable and great energy band gap match with the visible ranges [21].

Metal chalcogenides of a narrow bandgap have emerged as promising candidates for sensitising ZnO NRAs, among other applications. To fabricate photoelectrodes capable of exploit the features of both bandgap energy substances with a broad and a narrower bandgap while also enhancing the capacity for light harvesting of the hosting material, semiconductors metal chalcogenide with a narrow band gap, such as indium sulfide (In_2S_3) and lead sulfide (PbS) are being investigated. Electronic, optical, and semiconductor applications for metal chalcogenides with nanostructures are gaining attention. Aside from its stability and optical properties, In_2S_3 is a good candidate for this application due to its high absorption coefficients and appropriate band gaps (2.0–2.3 eV). This material is also non-toxic and readily available, unlike CdS and CdSe [22], which are both difficult to obtain. PbS is a toxic material, but it will be covered by In_2S_3 when ternary nanocomposite was formed in the end. When used as an infrared and visible absorber, PbS NPs had the highest solar AM 1.5G power-conversion efficiency for NPs photovoltaic devices [23]. PbS is a metal sulfide with potential photosensitive properties that may be synthesized in either the n or p form for solar energy applications. PbS nanomaterials can also absorb up to 40% of the solar radiation that reaches the earth's surface in the infrared region (wavelengths 800–1700 nm). As a result, PbS nanoparticles may improve light absorption [24]. The

use of semiconductor nanofilms based on materials composed of composites (i.e., bases with a narrow bandgap/metal oxide) has become increasingly important for improving the photoconversion's efficacy as a result of the strong conversions, flexibility, inexpensive of productions, and electrolyte system stability. Thin film nanomaterials are preferred due to their low cost of synthesis and low amount of starting materials required, which makes them suitable for large-scale manufacturing. The utilize PECs for the properties of nanocomposite materials which has the potential to drastically enhance (a) optimizing conditions for the manufacture of ZnO NRAs in try to integrate the photosensitizer; and (b) sensitising narrow band gap ZnO semiconductors, e.g., In_2S_3 and PbS , to boost absorption of additional visible light rays.

1.2 Problem Statement

ZnO is a significant candidate due to its high earth abundance and nontoxicity, in addition to its exceptional physical and chemical properties for a wide range of photovoltaic applications. When compared to other materials with wide bandgap energies, such as TiO_2 , its characteristics are excellent, with a 60 meV excitonic binding energy at room temperature and a bandgap energy of 3.37 eV. Because of this, it can only absorb a limited portion of the visible spectrum of light due to its wide band gap. The ability to increase visible light harvesting by sensitising the surface of ZnO NRAs has been presented in this study. Methods of sensitising the ZnO NRAs surface include doping organic dyes using nanocomposite materials or doping with narrow bandgap materials. After years of intensive research into organic dye sensitisation, researchers have turned their attention to inorganic metal chalcogenides with narrow bandgap energy values. This is due to their excellent absorption over a wide wavelength range, high stability, adjustable bandgap, and high conversion efficiency,

among other characteristics. There have been numerous studies that have demonstrated sensitisation of ZnO NRAs employing inorganic chalcogenide semiconducting nanoparticles, such as CdS [25], PbS [23], Ag₂S [14], Cu₂O [26], CdSe [27], and Bi₂S₃ [30, 31].

Metal chalcogenide narrow band materials can then be used effectively to improve the photo response of ZnO NRAs. Among the metal chalcogenide narrow band materials described above, indium sulfide (In₂S₃) and lead sulfide (PbS) are particularly effective. It is obvious that both In₂S₃ and PbS have suitable energy gaps within the visible light spectrum and can be considered appropriate materials for improving the light harvesting capabilities of ZnO solar cells. As a result, their high bandgap energy and narrow bandgap can effectively broaden the absorption range of ZnO from the ultraviolet to the visible light spectrum regions. Additional work has been done to cosensitise ZnO with the two narrow band metal chalcogenides to improve the alignment of the bandgaps, resulting in significant improvements in both electrical and optical properties. A significant issue that can arise when using sensitizer materials with narrow band gap energies is the massive percentage of electron-hole pairs recombination that occurs because of the high exciton binding energy.

In accordance with the findings of the literature review, further investigation into the performance of binary photoanodes of In₂S₃/ZnO and PbS/ZnO fabricated using the SILAR method is required to enhance the photoconversion efficiency of PEC. Currently, there is no information available on the deposition of the ternary construction of In₂S₃/PbS/ZnO to use it for photoelectrochemical applications. The synthesis of ZnO NRAs and nanocomposite samples was accomplished by a hydrothermal approach and the SILAR method. The two methods are simple, inexpensive, require little preparation time, have a low preparation temperature, have

controllable preparation parameters, and are environmentally friendly, all of which promote large-scale industrial production. This study makes a significant contribution to improving bandgap structure by employing binary and ternary nanocomposite for PEC application with simplified techniques.

1.3 Objectives

1. To improve the surface area of ZnO nanostructure layers by controlling the annealing temperature of the ZnO NPs seed layer by RF-magnetron sputtering and sol-gel spin coating, as well as the growth time of ZnO NRAs using hydrothermal method.
2. To enhance ZnO nanostructure's structural, optical and photoelectrochemical characteristics by depositing In_2S_3 and PbS as binary nanocomposite heterostructure into ZnO using the SILAR technique.
3. To fabricate and characterise In_2S_3 , PbS and $\text{In}_2\text{S}_3/\text{PbS}$ as co-sensitised ZnO nanorods to improve the alignment of bandgaps to achieve improved optical characteristics and photoelectrochemical efficiency.
4. To evaluate the photoconversion efficiencies of photoelectrochemical cells with different fabricated photoanodes ZnO NPs/ITO, ZnO NRAs/ITO, binary heterostructured $\text{In}_2\text{S}_3/\text{ZnO}/\text{ITO}$, $\text{PbS}/\text{ZnO}/\text{ITO}$, and ternary heterostructured $\text{In}_2\text{S}_3/\text{PbS}/\text{ZnO}/\text{ITO}$.

1.4 Significance of the Study

Increasing energy demand and limitations on existing energy sources, such as coal, oil, and natural gas, have caused a dramatic increase in the number of studies conducted on renewable energy sources that are abundant, environmentally sustainable, renewable, and cost-effective. Solar energy, when compared to the other

two most common sources of renewable energy, demonstrates the greatest potential. The energy radiated by the sun can be used to power the Earth for an entire year in only an one hour. A world map depicting horizontal solar irradiation globally demonstrates that sunlight has the potential to power almost every country's energy needs to meet their specific requirements. The rapid increase in research into solar energy has resulted in a few notable trends in recent years, which are discussed further in this paper. The effectiveness of the commercial panel has increased, while expenditures have decreased in proportion to this increase. Photoelectrochemical cells, based on photosensitised narrow-band materials, are considered to be one of the most important options for harnessing abundant solar energy due to their simple manufacturing and high photoconversion efficiency, among other advantages. As a result of this research, a significant contribution to the ongoing search for ZnO nanostructure sensitiser in order to improve light harvesting for photoelectrochemical applications would be made.

1.5 Scope of the Study

In this study, two different hierarchical hybrid materials are developed by simple SILAR method and their morphological structures, as well as effects of optical and electrical properties on the photoelectrochemical cells performance are investigated extensively. ZnO is used as a template for the growth of binary and ternary hierarchical nanostructures on ITO substrates. In all instances, the acquired heterostructure binary photoanode is fabricated through three basic steps: (i) preparation of high density ZnO nanoparticles seed layer via RF-magnetron sputtering and sol-gel spin coating; (ii) synthesising optimised well-aligned ZnO NRAs using simplified hydrothermal method; and (iii) photosensitising ZnO NRAs using narrow

bandgap energy metal chalcogenides with SILAR technique. The motivation of this research is to investigate the effect of In_2S_3 and PbS modifying the surface of ZnO NRAs on their performance as a photoanode in photoelectrochemical cells. Control of the production condition of $\text{In}_2\text{S}_3/\text{ZnO}$ NRAs/ITO, PbS/ZnO NRAs/ITO arrays, such as SILAR cycle number, dipping time, cationic concentration, and annealing temperature, is essential to enhance the ability of photosensitised-ZnO NRAs to harvest visible light.

1.6 Thesis Outline

This thesis is divided into six chapters. Chapter One includes the research background, problem statement, and objectives, followed by study significance and study scope. Chapter Two highlights the working principles of semiconductor electrodes in photoelectrochemical cells and related literature on methods of thin film synthesis heterostructure and characterisation techniques. Chapter Three outlines the methods and processes used in this study, with all the fabrication procedures for ZnO NPs/ITO seed layer, ZnO NRAs/ITO arrays, binary heterostructure ($\text{In}_2\text{S}_3/\text{ZnO}/\text{ITO}$, PbS/ZnO/ITO) and ternary structure ($\text{In}_2\text{S}_3/\text{PbS}/\text{ZnO}$ NRAs /ITO) and several preparations adjusting variables described and explained in detail. Chapter Four includes the data analysis and discussion of the findings and the outcomes of the experiments related to ZnO nanoparticles seed layers and ZnO NRAs. Chapter Five presents the data analysis and findings discussion of binary heterostructured photoanode ($\text{In}_2\text{S}_3/\text{ZnO}$ NRAs and PbS/ZnO NRAs/ITO) and includes the data analysis and discussion of results of the ternary heterostructure $\text{In}_2\text{S}_3/\text{PbS}/\text{ZnO}$ NRAs/ITO. Finally, Chapter Six presents the conclusions drawn from the research and makes recommendations for further related research.

CHAPTER 2

LITERATURE REVIEW

2.1 Introduction

Global warming and climate change are attracting attention as we progress in the twenty-first century. Clean and renewable energy sources have become increasingly important as the world's energy demand has increased and the availability of fossil fuels has decreased. A significant amount of research has been focused on renewable energy sources, such as solar, wind, and biofuels; however, another area of research that has seen significant expansion in recent years is the improvement of photoelectrochemical (PEC) cell conversion efficiency. This chapter covers the fundamentals of photoelectrochemical cells, semiconductor photoanodes, the characteristics and applications of ZnO, as well as some narrow bandgap energy metal chalcogenides, such as In_2S_3 , PbS and others that have been studied in the literature.

The science of materials is defined as the study of stable materials or condensed matter that establishes the relationship between the structure, characteristics, processing, and efficiency of a given material or condensed matter [30]. An interpretation of relationships promotes novel science since it results in the development of new products for high-tech implementations, ultimately leading to a higher quality of life. The fields of nanoscience and nanotechnology have continued to advance at a rapid pace throughout the world since their inception a few decades ago [30]. A wide range of human development applications involving nanomaterials have become one of the most exciting topics in science today. Scientific breakthroughs in nanomaterials have occurred in a variety of fields, including chemistry, physics, biology, and engineering, with the potential to determine the future of nanotechnology

advances in a wide and diverse range of fields. A nanomaterial's dimensions and size must be within the range of 1–100 nm in all dimensions and size, with no dimension smaller than one [31]. Various types of nanostructured materials, ranging from zero-dimensional to one-dimensional and two-dimensional to bulk nanomaterials, are essential for nanotechnology to function [32]. With respect to nanostructured materials, such as nanoparticles-quantum dots (zero dimensional), one-dimensional and two-dimensional, several significant properties are not typically present in the three-dimensional structure. When the spatial dimension and the effects of confinement within a structure are reduced in a given crystallographic direction, the physical features of the system alter in that direction [33]. This critical range of sizes is associated with a variety of intriguing phenomena that, in theory, follow the laws of nanoscience. In general, all materials can be divided into two groups based on their structural characteristics: the crystalline group and the noncrystalline group.

2.2 The Overview of Nanomaterials

The causes for such unique qualities of nanoparticles were gradually discovered as a result of the initial application of nanomaterials as pigments, in addition to the other unusual properties of nanomaterials [34]. This may be owing to the fact that they are small in scale but possess a large surface area. Certain rules of quantum mechanics come into play when an object's dimension is less than the average length of carriers, such as electrons and photons, resulting in the confinement of the carriers. In this scenario, energy levels are discretised and waves reveal their corpuscular nature. Furthermore, at the nanoscale level, objects have a very high surface area to volume ratio, and surface qualities dictate their behavior, which is said to be similar to that of free atoms, rather than being controlled by volume properties,

as is the case at the larger scale level of organisation [31]. To put it differently, the effects of gravity and inertia are rendered inconsequential when compared to the effects of electromagnetic forces and Van der Waals forces [35]. Similar to this, the impacts of nanoscale size and surface effects on the chemical, physicochemical, optical, electrical (including acoustic and magnetic), mechanical (including magnetic), and thermal properties of nanomaterials can be observed. In the case of metals and semiconductors, however, electrical properties at the nanoscale are governed by object dimensions that are smaller than the electron free mean path [36]. As a result, semiconductor nanoparticles have emerged as one of the most promising candidates for the fabrication of the working electrode in photoelectrochemical applications (PECs). ZnO is another semiconductor that has been extensively employed in PEC applications, such as photovoltaics and photocatalysis, as it is one of the most abundant semiconductors available. Several studies have been conducted in order to find economical synthesis methods for ZnO nanostructures with the desired qualities in order to improve the performance of PECs, and the results have been promising [37].

2.2.1 Metal-Oxide Nanostructures with a 1D Structure

The width and thickness of the 1D (one-dimensional) nanostructures are limited to the nanoscale, but the distance can be several millimeters or more, resulting in extremely high aspect ratios [38]. Notably, as 1D nanostructure get smaller, their electrical properties diverge from the bulk materials, causing slight changes in chemical and physical properties. 1D metal-oxide nanostructures are regarded as synthetically tunable building blocks for electronic devices and functional systems of the future due to their high aspect ratio, single crystal properties, precise control of

composition and structure, and directed mobility of charge carriers [39]. ZnO is one of the most important 1D metal-oxide semiconductor nanostructures. Zinc oxide NRAs have gained popularity in recent decades, particularly in bio-sensing and optoelectronic devices. Whiskers [40], fibres [41], nanowires [42], nanorods [43], and nanotubes are some of the features that can be found in 1D ZnO nanostructures [44]. Due to size confinement in one dimensions, nanorods are often favoured.

2.2.2 Heterostructured-Semiconductor

Heterostructures are the foundation of modern semiconductor devices. They are essential in high-efficiency optical sources and detectors, as well as optoelectronic systems. Heterostructured semiconductors have distinct electrical and optoelectric capabilities due to structures made of two semiconductor materials in junction contact. A heterojunction is a crystal junction produced by two distinct semiconductors, with the energy gap and refractive index being the main distinctions between them [45]. Energy gap differences allow for the spatial confinement of injected electrons and holes in semiconductor heterostructures, whereas variances in refractive indexes can be exploited to generate optical wave paths. Heterostructured semiconductors have also been used in diode laser devices, light emitting diodes [46], optical detector diodes, photoelectrochemical cells, and solar cells. Understanding the physical properties of the heterojunction is critical for its effective use in applications. The energy band alignment is the most fundamental attribute of a heterojunction, which influences the suitability of various material combinations for specific application devices. The band alignments are topologically categorised into three types, depending on the relative order of the band difference energies, as shown schematically in Figure 2.1.

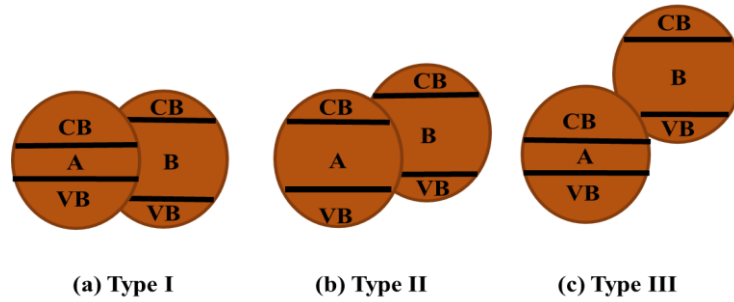


Figure 2.1 A diagram depicting the heterostructured-alignment process, with C.B. and V.B. representing the valence and conduction bands, respectively. (a) Type I band alignment, "straddling," (b) Type II staggered gap, and (c) Type III broken gap

Straddling configuration is the most common or standard alignment in which the bandgaps do not completely overlap; one of the semiconductors' bandgaps (lower bandgap semiconductor) lies below the bandgap of another semiconductor [47]. Within this type of structure, all forms of charge carriers, i.e., electrons and holes, are restricted to the heterojunction due to the presence of the potential barrier at the interface. The smaller bandgap material's conduction band may be higher than that of the larger bandgap material, or its valence band may be lower than that of the larger gap material. This type of energy description is known as a "staggered" arrangement. As a result, with this structure, any charge carrier will encounter a potential barrier at the interface, limiting just one type of charge carrier to the heterojunction [48]. When the staggering becomes so severe that the bandgaps no longer overlap, the condition is known as "broken configuration," which is also known as "misaligned configuration". Heterostructures of type III function as either a material with a narrow gap or a material with a zero gap (semi-metal). These semiconductor heterostructures are also key components in the construction of optoelectronic devices, where the ability to tolerate optical radiation is critical. The band offsets are equivalent to the possible obstacles encountered by the carrier during band alignment (type I and type

II). The appropriateness of Type I structures is highly recommended in developing semiconductor lasers, whereas Type II structures are reported to be an excellent contender in terms of material for designing "avalanche photodetectors" in which only one type of carrier velocity is the accepted optical communication devices which are intended in a wavelength range of 1.33-1.55 μm , whereas smaller wavelengths are more flexible. ZnO-based heterostructures are in demand due to their broad bandgap energy of 3.37 eV and related shorter emission wavelength, as well as their high exciton binding energy of roughly 60 meV. It is widely known that semiconductor chalcogenide bases placed on ZnO, such as CdS [49], In_2S_3 [50], Ag_2S [51], PbS [52], and Bi_2S_3 [53], lead to E_g reduction via the Type-II heterostructure.

2.3 Photoelectrochemical Cell

Solar energy is collected and converted using a variety of technologies, including photovoltaic (PV), photoelectrochemical (PEC), and photothermal cells [37,54]. In terms of mode of action, PV and PEC are fundamentally identical (light absorption, charge carrier creation and separation). A p–n homojunction or heterojunction generated from doped or inherent semiconductors that are also light-absorbing phases is typical in a PV device. In a PEC device, the junction is typically created between a semiconductor electrode and an electrolyte solution. The PEC is defined as "one in which the irradiation of the electrode/electrolyte system induces a change in the electrical potential (on the open circuit) or the external current flowing circuit (under short circuit conditions)" [7]. The electrolyte semiconductor interface has been used to directly convert the sun spectrum to electrical energy [55]. Quantum efficiency and long-term stability are two critical elements to consider when employing PEC for considerable effective conversion efficiency [56]. When working

in the right electrolyte, semiconductor electrode materials should be able to catch a significant portion of the visible light spectrum and exhibit acceptable stability [57]. However, these two objectives are contradictory, as in most circumstances, the narrower the bandgap, the more susceptible the semiconductor is to photochemical corrosion. Extensive research has been conducted to build solar cells in the form of solar fuel for converting solar energy into chemical energy and ultimately electrical energy. The goal is to create PEC that divide water into hydrogen using oxygen as a byproduct. This technology is appealing for the reasons stated above [58].

2.3.1 Photoelectrochemical Cell Fundamental Principles

The PEC efficiency is highly dependent on the photoanode material's properties, such as charge carrier separation, visible light harvesting ability, charge carrier transportation, and the structure. A PEC cell's core is the photoanode semiconductor. As a result, the overall performance of PEC is primarily determined by the material used to make the semiconducting electrode and its parameters. The following requirements must be met to achieve a good performance:

- A good photoanode should be able to absorb light from a wide range of wavelengths across the solar spectrum, and a high surface-to-volume ratio photoanode will optimise photoinduced charged carrier absorption.
- Semiconductor photoelectrode materials should have a high optical absorption coefficient. Photoanode crystallinity is crucial for PEC photoconversion. Oriented crystalline structures perform photoconversion better than amorphous materials [59].

- The photoelectrode material's bandgap (E_g) should be as narrow as feasible to match the solar spectrum ($E_g = 1.2-1.8$ eV). Direct band gap devices with high optical absorption coefficient (α) outperform indirect band gap structures [60].
- Minority carriers should be diffused for as long as possible to maximise coverage. The width of the space charging layer must be substantial. It should be steady and have a high electrolyte resistance under illumination, as well as also be free of corrosion.
- The photoelectrodes' thickness and surface area should be sufficient to absorb enough incident radiation for the specified function. The photoanode to electrolyte charge transfer resistance (R_{ct}) should be kept to a minimum. The working electrode synthesis process must be inexpensive and eco-friendly [61].

Another critical parameter in a PEC solar cell is the electrolyte. An electrolyte is a solution that acts as a conductor of electricity. The molecules that are oxidised and reduced are found in electrolytes, and are known as ionic species that aid in the movement of photogenerated holes from the photoelectrode to the counter electrode [62]. The performance of a PECs cell should be satisfactory if the electrolyte meets all of the following requirements [63]:

- The redox system's transfer charging rates must be high or effective at both the semiconductor working and counter electrodes, and the electrolyte must have the lowest optical absorption possible.
- Oxidised species, as well as solvent components, should exhibit high thermal and photo stability over the visible light spectrum and ambient temperature range. A non-corrosive electrolyte is required for the semiconductor working electrode and the container.

- The pH of the electrolyte is critical to its effective performance in PECs. Consideration should be given to cost, toxicity, and environmental impact. Nanomaterials combined with a photoanode exhibit stability over a wide pH range.

The photoelectrochemical cell's third component, the counter electrode, is just as critical as the other components that have been demonstrated. When selecting a counter electrode, many factors must be taken into account to achieved the desired photoconversion efficiency [64].

- A fast charge transfer between the counter electrode and the electrode redox species should be achieved by using an electrically active counter electrode.
- The counter electrode surface area must be greater than the semiconductor electrode surface area to improve photogenerated electron collection and avoid polarisation when a counter electrode is immersed in the electrolyte. The counter electrode should be cheap, such as graphite and platinum wire (Pt). Moreover, it must not react with the electrolyte.

There are numerous advantages of semiconductor/liquid junction cells over solid-state junction cells that contribute to their appeal. The junction is formed by simply immersing the semiconductor in the liquid. Additionally, electron–hole pairs are formed in a high-field region, allowing for efficient charge separation. PECs are economically advantageous when compared to conventional solid-state junction solar cells [7]. Band bending of the semiconductor photoelectrode can occur following electrode immersion in the electrolyte. Electron transmission from the electrolyte is limited to the conduction band energy region, whereas hole transitions occur in the valence band energy region. This transition may occur between two states with nearly identical energy levels, one vacant and one filled. Electron-hole pairs are formed in

the depletion layer under the influence of illumination, and are separated by the electrical field of the interface. The energy of the incident photon must exceed that of the semiconductor's bandgap energy. Typically, the electron-hole pairs formed in the bulk of semiconductors are lost due to recombination. When a positive potential is applied to the photoelectrode and illuminated n-type semiconductor, electron-hole pairs are formed, and divided electrons begin to ascend to the conduction band, while holes transfer to the valence band [37].

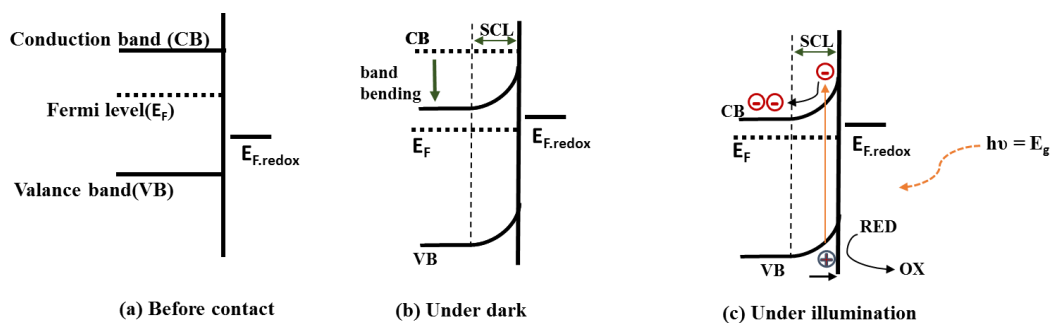
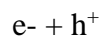


Figure 2.2 Energy band diagram for a n-type semiconductor

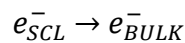
The performance of charged carriers in a semiconductor in contact with an electrolyte is demonstrated in Figure 2.2. For n-type semiconductors and electrolytes, the potential difference between the electrode's surface and bulk is zero, indicating the absence of a space charge layer. The potential is referred to as "flat-band potential, V_{fb} " if the band's edges are perfectly flat. By applying a potential significantly greater than the potential of a flat band, one can increase the band bending at an n-type semiconductor electrode, such as ZnO. The electrons are drastically reduced in this case, while the holes at the surface are enriched, as illustrated in Figure 2.2. When the working electrode is irradiated, it is demonstrated that the photogenerated holes have an oxidising effect equal to the valence band edge potential and can easily oxidise the redox molecule, which has a more negative formal potential than the valence band. In

the case of ZnO, the H₂O can be oxidised to form OH⁻ radicals. The electron in the conduction band travels to the counter electrode through an external circuit, such as reducing H⁺ ions to H₂, may occur. It is critical to note that the faster the (electron-hole) pairs are separated in the photoelectrochemical cell, the greater the band-bending and the space charged layer (SCL), and thus, less charge recombination occurs. Different steps, involved in a n-type semiconductor photoelectrochemical cells, can be explained as follows:

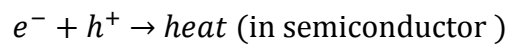
(1) Absorption of light by the working electrode:



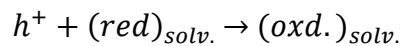
(2) The separation of electrons and holes in the space charging layer (SCL)



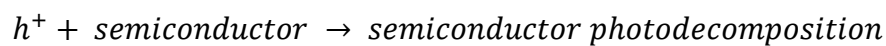
(3) Bulk electron-hole recombination



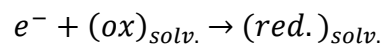
(4) Redox species interact with holes on the surface of semiconductors.



(5) Surface holes on semiconductors have the potential to react with the semiconductor bands themselves.



(6) The reduction of redox species in comparison to the counter electrode.



Photogenerated carriers are limited by reactions (3), (5), and (6). PEC solar cell performance can be further improved by reducing surface states and recombination in the space charge layer [63].

2.3.2 Quantum Confinement Theory on the Nanoscale

The properties of materials with nanoscale structures are usually unique in terms of their optical, electronic, or mechanical properties. Structures of sizes comparable to a wide range of possible length scales will inevitably have novel effects on materials. When an ultra-short length scale directly impacts the bandgap energy structure at ultra-small length scales, the quantum confinement effect is a term that is frequently heard in the nanoscience [65]. 1 to 25 nm is a good fit for quantum confinement schemes for standard semiconductor groups, such as IV, III, and II. The electronic wave function's spatial range corresponds to the particle size. Electrons respond to boundaries and changes in particle size by changing their energy, a phenomenon known as the quantum-size effect, in accordance with this geometric constraint. Quantisation effect is significant, and the particle size of semiconductors should always be equal to or less than the bulk exciton Bohr radius of the semiconductor. The Bohr radius of a particle is generally defined as follows [66,67]:

$$\alpha B = \epsilon \frac{m}{m^*} a_o \quad (2.1)$$

where: α is the fine structure constant, B is Bohr radius of the particle, ϵ is the material's dielectric constant, m is the rest mass of the electron, m^* is the mass of the particle and a_o is the Bohr radius of the hydrogen atom. Quantum confinement increases excitonic transition energy and blue shifting in absorption and optical bandgap energy, provided that the particle size is nearly equal to Bohr's exciton radius [69, 70]. Discrete, atomic-like energy levels may also be formed as a result of quantum confinement of the bulk material's continuous energy bands. Thus, the discrete structure of energy state results in a discrete spectrum of absorption, which differs from the continuous spectrum of a bulk semiconductor. The carrier's motion of the

electron and the hole is restricted in one or more directions by the behavior of the potential barriers in a quantum confined structure [69]. The electron's environment can be reduced from a two-dimensional quantum well to a one-dimensional quantum wire and finally to a zero-dimensional quantum dot. An electron in a quantum wire is confined to two directions rather than one, as in a quantum well, thus reducing the degrees of freedom to one. As the electron is confined in all three dimensions, there are no degrees of freedom. If D_f is the number of degrees of freedom and D_c is the number of directions of confinement, then constrained quantum structures are stated as shown in Table 2.1.

$$D_f + D_c = 3 \quad (2.2)$$

Table 2.1 Quantum confined structure classification.

Structure	Degree of Confinement (D_c)	Degree of freedom (D_f)
Bulk Material	0D	3D
Quantum Well	1D	2D
Quantum Wire	2D	1D
Quantum Dot	3D	0D

QDs contain charged carriers in all three dimensions. When the system is restricted to two dimensions, the electrons exhibit a distinctive atomic-like energy spectrum and the formation of quantum wires. There is no limit to the number of electrons and holes (charge carriers) that can be transferred, as they can also move freely in two dimensions. One of the quantum numbers is experiencing a shift from continuous to discrete energy. The electronic state near the conductive and valence band edges is denser in quantum wells than it is in bulk semiconductors. In this way, the band edge emission can be amplified by a larger number of carriers. Carrier movement is restricted to a single dimension, implying that as more dimensions are confined, more distinct amounts of energy are likely to be discovered. Clearly defined and quantified energy levels in 0D structures can be observed. The particle size and

size-dependent nanoparticle properties for spatially confined nanostructures are calculated using the Effective Mass Approximation (EMA) [70].

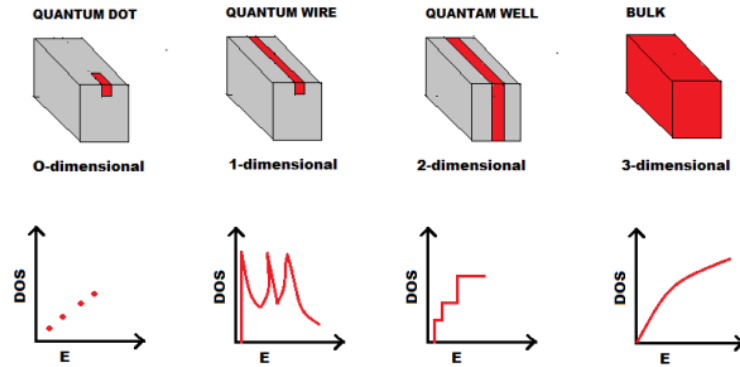


Figure 2.3 Quantum confinement of 0D, 1D, 2D, and 3D nanostructures with density of states (DOS) effects

If the particle size is minynte and not equal to the wavelength of the electron, the effect of quantum confinement is observed at this stage. To clarify, the terminology is divided into "quantum" and "confinement". Confinement means "to restrict the motion of a randomly moving electron in specific energy levels," whereas quantum "reflects the atomic realm of particles." Thus, confinement means "trying to restrict the movement of a spontaneously moving electron in different energy levels," whereas quantity "reflects the atomic domain of particles." As a result, when the particle size is reduced to a nanoscale, the confining dimension is reduced, making the energy levels discrete. This causes the bandgap to expand, consequently increasing the bandgap of the nano-structured semiconductor.

2.4 Characteristics of Zinc Oxide (ZnO)

Zinc oxide, abbreviated ZnO, is a semiconductor compound belonging to the II-VI group with a diverse range of unique properties. It is an n-type semiconductor with a large direct bandgap, a large exciton binding energy, and a large piezoelectric constant [71]. It is transparent in the visible region but absorbs a significant amount of electromagnetic radiation in the UV-Blue range [72]. Due to their superior piezoelectric and pyroelectric properties, ZnO nanostructured materials have garnered considerable interest in electronics, optics, and photonics applications [13]. This is ideal for optoelectronic applications requiring a short wavelength with a relatively wide and direct bandgap (3.37 eV) [72,73]. The high exciton binding energy at room temperature (60 meV) enables efficient excitonic emission and may be desirable for photonic applications [18,74].

Numerous reports have demonstrated the use of ZnO nanostructures in a variety of applications, including gas sensors. To name a few, these include nanoparticles [75], biosensors [76], light emitting diodes (LEDs) [77], transparent electrodes [78], solar cells [72,79] and photoelectrochemical cells (PECs) [82, 83]. Another significant property of ZnO is its diverse family of ZnO nanostructures, which includes nanorods [73], nanobelts [82], nanoflowers [76], and nanowires [83]. ZnO is a remarkable n-type semiconductor that crystallises in three distinct forms, as illustrated in Figure 2.4: hexagonal wurtzite, cubic zinc blend, and rock salt. Under ambient conditions, ZnO crystallises in the most stable hexagonal wurtzite structure with lattice spacing $a = 0.325$ nm and $c = 0.521$ nm.